Surface morphology of $CuFeS_2$: The stability of the polar (112)/($\overline{1}\overline{1}2$) surface pair

Vincent H.-Y. Chen,[1] Giuseppe Mallia,[2] Ruth Martínez-Casado,[3] and Nicholas M. Harrison[2,4,*]

[1]*Department of Physics, Imperial College London, South Kensington, London SW7 2AZ, United Kingdom*

[2]*Department of Chemistry, Imperial College London, South Kensington, London SW7 2AZ, United Kingdom*

[3]*Department of Theoretical Condensed Matter Physics, Autonomous University of Madrid, 28049 Madrid, Spain*

[4]*Daresbury Laboratory, Daresbury, Warrington WA4 4AD, United Kingdom*

(Received 13 July 2015; revised manuscript received 15 September 2015; published 21 October 2015)

The reconstruction and energetics for a range of chalcopyrite ($CuFeS_2$) surfaces have been investigated using hybrid-exchange density functional theory. The stable nonpolar surfaces in increasing order of surface energy are (110), (102), and (114). In addition, the polar (112)/($\overline{1}\overline{1}2$) surface pair was found to be remarkably stable with a surface formation energy that is only slightly higher than that of the (110) surface. The stability of (112)/($\overline{1}\overline{1}2$) can be attributed to a combination of geometric and electronic mechanisms that result in the suppression of the electrostatic dipole perpendicular to the surface. Defect formation is a third mechanism that can further stabilize the (112)/($\overline{1}\overline{1}2$) surface pair to an extent that it is thermodynamically preferred over the (110) surface. The stability of (112)/($\overline{1}\overline{1}2$) means that regardless of the growth conditions, (112) and ($\overline{1}\overline{1}2$) facets are expected to have a significant presence in the surface morphology of $CuFeS_2$.

DOI: 10.1103/PhysRevB.92.155426 PACS number(s): 71.15.Mb, 68.35.Md, 05.70.Np

I. INTRODUCTION

Chalcopyrite ($CuFeS_2$) is the most abundant copper-bearing mineral, accounting for ~70% of the world's copper reserves [1,2]. Pyrometallurgy, which involves heat-intensive techniques such as smelting, is currently the predominant method for extracting copper from $CuFeS_2$ but is only economical for treating high-grade ores on a large scale due to high capital and operational costs [3,4]. Furthermore, smelting leads to the emission of sulfur dioxide gas, toxic chemicals, and other particulate matter that can cause health and environmental problems [3]. With the progressive depletion of high-grade chalcopyrite ores, the inefficiency of pyrometallurgical extraction for low-grade ores, and its potential harmful associated side effects there is a growing need for the development of alternative extractive processes [3].

Hydrometallurgy, which involves solution-based extractive techniques such as heap leaching and bioleaching, is considered a viable alternative to pyrometallurgy due to lower startup and operational costs [5,6]. Furthermore, with no harmful gas emissions, hydrometallurgy is less environmentally hazardous than pyrometallurgy, although care must be taken to ensure stabilization of the final leaching residue prior to disposal [2]. Despite several successful demonstration plant operations, the hydrometallurgical processing route is currently not industrially feasible for the extraction of Cu from $CuFeS_2$ as the leaching stage suffers from poor dissolution kinetics, ultimately resulting in uneconomical yields [2].

Over the last few decades, research on the hydrometallurgical extraction of Cu from $CuFeS_2$ has mainly involved carefully controlled experimental leaching studies, with the ultimate aim of economical implementation on an industrial scale. It is generally agreed that the formation of a passivation layer is to blame for the significant retardation in the copper dissolution rate; however, consensus is achieved neither on the nature of the film nor on details of the associated surface chemistry [1]. Numerous candidate species responsible for passivation have been proposed, such as elemental sulfur (S_8) [7,8], polysulfides (XS_n) [9], and jarosites [$XFe_3(SO_4)_2(OH_6)$] [10].

Experimental studies of $CuFeS_2$ surfaces thus far have been able to determine only elemental composition but not details of the surface morphology. It has consequently not been possible to establish the structure and composition of crystallite surfaces or to determine which facets are typically exposed in small crystallites. This is mainly due to the fact that $CuFeS_2$ exhibits very poor cleavage, which means that any fracture will result in a variety of surfaces being exposed [11,12]. We have therefore performed *ab initio* calculations of $CuFeS_2$ surfaces in order to establish realistic models of the surface structure, formation energies, and crystallite morphology of $CuFeS_2$.

$CuFeS_2$ adopts a tetragonally coordinated (space group: $I\bar{4}2d$) zinc-blende-like structure, shown in Fig. 1, where each anion (S) is bonded to four cations (2 Cu and 2 Fe) and vice versa. The optimized lattice parameters were obtained from our *ab initio* characterization of bulk $CuFeS_2$ [13], which employed the same approach used here, and differ only slightly (~3%) from experimental values [14], as shown in Table I. The slight overestimation is typical for bond lengths of ionic materials calculated using the hybrid-exchange Becke three-parameter Lee-Yang-Parr (B3LYP) approximation to density functional theory.

Tasker formally devised a scheme to classify surfaces of ionic crystals based on the ionic model and the geometric distribution of cations and anions in the surface unit cell [15]. Surfaces of type 1 or 2, whose repeating units have no electrostatic dipole moment perpendicular to the surface, are typically stable with a modest surface energy and only limited relaxation or reconstruction of surface atoms. Conversely, type-3 surfaces, whose repeating units have a net electrostatic dipole moment perpendicular to the surface, have surface energies divergent with sample size unless the dipole is quenched by reconstruction, charge transfer, or chemical mechanisms.

For zinc-blende semiconductors such as GaAs and ZnSe, which adopt a tetrahedrally coordinated structure similar to

*nic.harrison@imperial.ac.uk

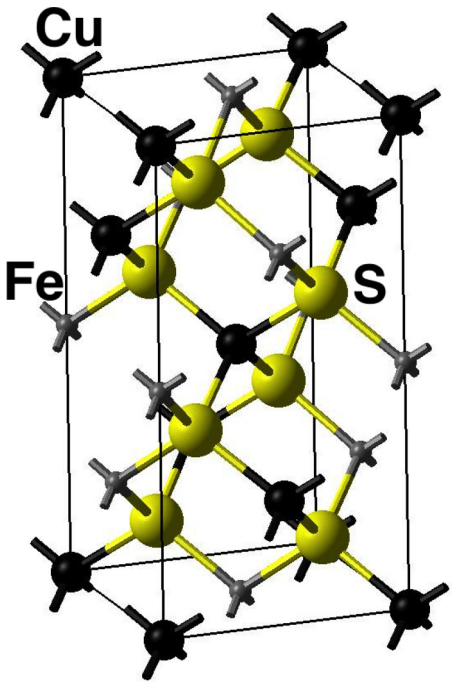

FIG. 1. (Color online) The conventional unit cell of bulk $CuFeS_2$.

that of $CuFeS_2$, the nonpolar (110) surface is usually the lowest in energy [16–18]. Intriguingly, various theoretical studies have shown that the nonpolar vs. polar stability trend is reversed for $CuInSe_2$, a $A^{I}B^{III}X_2^{VI}$ semiconductor isomorphic to $CuFeS_2$. Jaffe and Zunger performed density functional theory (DFT) calculations in the local density approximation (LDA) and predicted that the presence of point defects can lower the energy of the polar (112)/$(\overline{1}\overline{1}2)$ surface pair so that it is considerably lower in energy than the nonpolar (110) surface under particular growth conditions [19]. They reported that the (1×1) surface pair is stabilized by a Cu vacancy on the $CuInSe_2$ (112) cation-terminated surface under Cu-poor conditions or by a Cu-on-In antisite defect on the same surface under In-poor conditions. Their conclusions were replicated in similar DFT-LDA calculations by Zhang and Wei, who further predicted thermodynamic stability of the (112)/$(\overline{1}\overline{1}2)$ surface pair, with a Se addimer at $(\overline{1}\overline{1}2)$, with respect to the (110) surface [20]. Stability of the polar (112) and $(\overline{1}\overline{1}2)$ $CuInSe_2$ facets is also evident experimentally. Spontaneous decomposition of the (110) surface into (112)/$(\overline{1}\overline{1}2)$ polar facets has been observed during epitaxial growth [21]. It is possible that this defect-induced stabilization mechanism is of general relevance to systems containing two cation species with different formal oxidation states such as compounds of the $A^{I}B^{III}X_2^{VI}$ family.

TABLE I. Structural parameters (in angstroms) of optimized bulk $CuFeS_2$ compared with experimental values [14].

	Current work	Experiment
a	5.452	5.289
c	10.710	10.423
d_{Cu-S}	2.395	2.302
d_{Fe-S}	2.300	2.257

It is only recently that surfaces of $CuFeS_2$ have been investigated theoretically. Von Oertzen *et al.* performed DFT calculations in the generalized gradient approximation (GGA) on the nonpolar (012) surface and the polar $(11\overline{2})$ surface [11]. They concluded that the (012) surface is extremely unstable with a very irregular relaxed structure while the metal-terminated $(11\overline{2})$ surface undergoes dramatic relaxation resulting in the exposure of S in the form of disulfide species. De Oliveira and Duarte performed DFT-GGA calculations to investigate the geometry and electronic structure of the relaxed sulfur- and metal-terminated nonpolar (001) surfaces [22]. Their analysis predicted oxidation of S^{2-} to S^{-} coupled with reduction of Fe^{3+} to Fe^{2+} at the surface, leading to the formation of surface disulfide S_2^{2-} and iron disulfide Fe_2S_2 phases, which have also been observed experimentally using x-ray photoelectron spectroscopy (XPS) [23,24]. De Oliveira *et al.* reached similar conclusions using DFT-GGA calculations on an expanded set of nonpolar surfaces [25]. The adsorption of water, sulfuric acid, and hydrochloric acid on the relaxed $CuFeS_2$ (001) surface has also been investigated [26,27]. To the best of our knowledge there are no published studies of polar $CuFeS_2$ surfaces providing a comprehensive survey of low-index surfaces and the effect of defects. In order to thoroughly understand the surface morphology of $CuFeS_2$, in the current work we have performed *ab initio* calculations beyond the LDA and GGA level on a variety of its surfaces, mostly nonpolar surfaces but also the polar (112)/$(\overline{1}\overline{1}2)$ surface pair with various surface defect formations.

II. METHOD

Spin-polarized DFT calculations were performed using the CRYSTAL09 software package based on the expansion of crystalline orbitals as a linear combination of a local basis set (BS) consisting of atom-centered Gaussian orbitals [28,29]. The copper, iron, and sulfur atoms were described by a triple-valence all-electron BS: an 86-4111G** contraction (one s, five p, and two d shells), an 86-4111G** contraction (one s, five p, and two d shells), and an 86-311G* contraction (one s, four p, and one d shells), respectively. This BS was deployed and shown to be adequate in our study of $CuFeS_2$ bulk, which confirmed that the ground state of $CuFeS_2$ is antiferromagnetic [13].

Electronic exchange and correlation was approximated using the hybrid-exchange B3YLP functional [30,31], chosen because it has shown to reliably describe the geometry, energetics, and electronic properties of bulk $CuFeS_2$ [13] and a wide range of other strongly correlated systems [32–39]. In particular, the B3LYP functional better predicts the band gaps of semiconductors than functionals based on the local density or generalized gradient approximations [40–42]. Matrix elements of the exchange and correlation potentials and the energy functional are integrated numerically on an atom-centered grid of points. The integration over radial and angular coordinates is performed using Gauss-Legendre and Lebedev schemes, respectively. A pruned grid consisting of 99 radial points and 5 subintervals with (146, 302, 590, 1454, and 590) angular points has been used for all calculations (the XXLGRID option implemented in CRYSTAL09 [28,29]). This grid converges the integrated charge density to an accuracy

of about 10^{-6} electrons per formula unit. The Coulomb and exchange series are summed directly and truncated using an overlap criterion with thresholds of 10^{-7}, 10^{-7}, 10^{-7}, 10^{-7}, and 10^{-14} as described previously [29,43]. Reciprocal space sampling for all surfaces was performed on a Monkhorst-Pack net with a shrinking factor of 4 in each periodic direction, generating ten k points in the irreducible Brillouin zone (IBZ).

A systematic approach was employed to screen the surfaces investigated down to a manageable number for this work. It is important to note that the surfaces in this investigation are modeled using slabs where both terminations are relaxed simultaneously. Depending on the cleavage plane, the resulting slab may be asymmetric, which means the two surfaces of the slab are different. Such slabs are denoted using the term "surface pair." Initially, we considered all stoichiometric slabs generated from cleaving the bulk crystal along planes with small Miller indices ($h, k, l \leqslant 3$). Using the ionic model with the formal charges of $CuFeS_2$ (+1, +3, and −2 for Cu, Fe, and S respectively), the electrostatic dipole perpendicular to the surface for each of these slabs was calculated to classify the surfaces and surface pairs into nonpolar and polar types. All polar slabs were filtered out, leaving a list of nonpolar slabs which were then ranked in ascending order of bonds broken as a result of cleaving the bulk scaled by surface unit area. The top ten slabs of the ranked list, representing surfaces or surface pairs with relatively few undercoordinated surface atoms, were further considered. These are the $(212)/(\overline{212})$, $(213)/(\overline{213})$, $(322)/(\overline{322})$, $(323)/(\overline{323})$, $(223)/(\overline{223})$, (102), (110), $(313)/(\overline{313})$, $(111)/(\overline{111})$, and $(221)/(\overline{221})$ surfaces and surface pairs whose respective Tasker classifications are types 2, 2, 2, 2, 2, 1, 1, 2, 2, and 2. Note that for all surface pairs, the atomic layers of their repeating units are not symmetric, but because the electrostatic dipole moments perpendicular to the surface are zero, they are (nonpolar) type 2. The geometry of these ten slabs was further inspected, and slabs with surface geometric features that are likely to be chemically unstable were eliminated from the investigation. As an example, the $(111)/(\overline{111})$ surface pair shown in Fig. 2 was eliminated as it has one singly coordinated S atom on the $(\overline{111})$ surface per unit cell. Indeed, a test DFT calculation performed on the $(111)/(\overline{111})$ slab resulted in failed convergence of the wave function during the self-consistent field (SCF) procedure. The remaining slabs, representing the (110) and (102) surfaces, both Tasker type 1, were investigated in this work. In addition, the nonpolar (114) surface, also a Tasker-type-1 surface, was investigated as it was reported to be stable from DFT-GGA calculation performed by de Oliveira *et al.* [25]. It may be possible that slabs eliminated during the filtering process can be stable in larger periodicities through the formation of complex reconstruction patterns. However, this is beyond the scope of this investigation, which is limited to the consideration of (1×1) surface unit cells.

In addition to the nonpolar surfaces, the polar cation-terminated (112) and anion-terminated $(\overline{112})$ [referred to as $(112)/(\overline{112})$ from here on] surface pair was also investigated because its $CuInSe_2$ counterpart has been shown to be thermodynamically stable with particular combinations of defect(s) and growth conditions from DFT-LDA calculations [19,20]. Eight different defect configurations of the surface pair were investigated. These are (a) the defect-free surface pair, (b) two

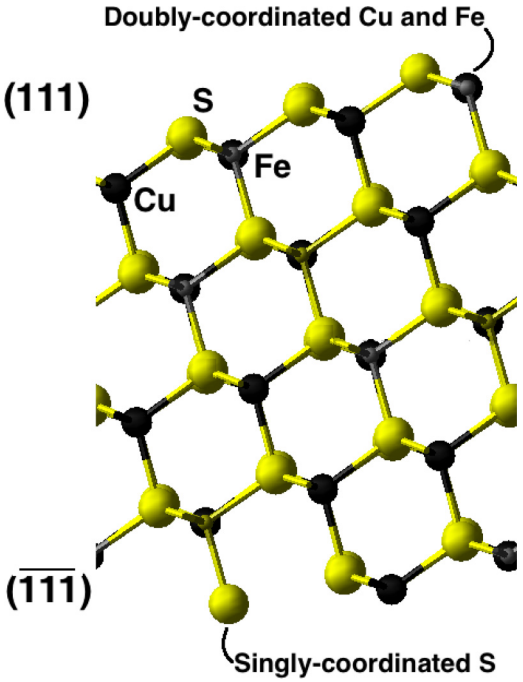

FIG. 2. (Color online) The unrelaxed nonpolar $(111)/(\overline{111})$ slab. The most undercoordinated atoms are labeled.

Cu vacancies on the (112) surface, (c) a Cu, Fe vacancy pair on the (112) surface, (d) a Cu-on-Fe antisite on the (112) surface, (e) a Fe-on-Cu antisite on the $(\overline{112})$ surface, (f) a S adatom on the $(\overline{112})$ surface, (g) a S addimer on the $(\overline{112})$ surface, and (h) a Cu, Fe vacancy pair at the (112) surface and two S vacancies at the $(\overline{112})$ surface. Systems (b) to (g) were chosen because their $CuInSe_2$ counterparts were predicted to be stable based on calculations by Jaffe and Zunger and Zhang and Wei [19,20]. System (h) was constructed in order to maintain "macroscopic stoichiometry" at both terminations based on the generalization of surface polarity by Finnis [44].

For all slabs, a constant thickness of roughly 10 Å was employed because that was shown to be sufficient in the case of the nonpolar (110) and the defect-free polar $(112)/(\overline{112})$ slabs for the surface energy to be converged to within 0.01 J m^{-2} and for the surface Mulliken charges to be converged to within $0.01|e|$.

Geometry optimization of the slabs was performed *in vacuo* with two-dimensional periodic boundary conditions starting from the bulk configuration using the Broyden-Fletcher-Goldfarb-Shanno scheme, as implemented in CRYSTAL09 [28,29]. The movement of all atoms was unrestricted during all optimizations. Convergence was determined from the rms and the absolute value of the largest components of forces and atomic displacements. The thresholds for the maximum and rms forces were set to 0.00045 and 0.00030, while those for the atomic displacements were 0.0018 and 0.0012, all in atomic units. Geometry optimization was terminated when all four conditions were satisfied simultaneously. Ionic charges were determined using a Mulliken partition of the total charge density, as implemented in CRYSTAL09 [28,29].

For nonstoichiometric configurations of the polar $(112)/(\overline{112})$ surface pair, the surface formation energies were

TABLE II. Seven sets of chemical potential values bound to the constraint $\mu_{Cu} + \mu_{Fe} + 2\mu_S = -1.8$ eV, representing a wide range of growth conditions.

Condition	μ_{Cu} (eV)	μ_{Fe} (eV)	μ_S (eV)	Description
A	−1.8	0.0	0.0	Cu poor
B	−0.9	−0.9	0.0	S rich
C	−0.6	0.0	−0.6	Fe rich
D	−0.45	−0.45	−0.45	Balanced
E	0.0	−1.8	0.0	Fe poor
F	0.0	−0.6	−0.6	Cu rich
G	0.0	0.0	−0.9	S poor

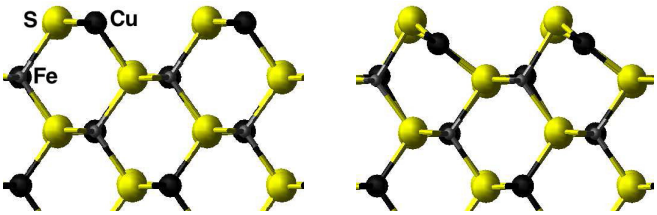

(a) Unrelaxed (b) Relaxed

FIG. 3. (Color online) (a) The unrelaxed and (b) relaxed nonpolar (110) surface. The (110) surface is at the top, and the bulklike region is at the bottom.

calculated within a grand-canonical formulation. Defining the atomic chemical potential for each species (μ_{Cu}, μ_{Fe}, and μ_S) relative to its pure bulk phase, the surface formation energy of a slab E_{surf} is

$$E_{surf} = \Delta E + n_{Cu}\mu_{Cu} + n_{Fe}\mu_{Fe} + n_S\mu_S, \quad (1)$$

where

$$\Delta E = E_{sys} - N E_{bulk}(CuFeS_2) + n_{Cu} E_{bulk}(Cu) + n_{Fe} E_{bulk}(Fe) + n_S E_{bulk}(S). \quad (2)$$

Here, E_{sys} is the total energy of the slab, and $N E_{bulk}(CuFeS_2)$ is the energy of the equivalent amount of bulk $CuFeS_2$. $E_{bulk}(Cu)$, $E_{bulk}(Fe)$, and $E_{bulk}(S)$ are the calculated bulk energy per atom of Cu(fcc), Fe(bcc), and S_8(molecule), respectively. n_{Cu}, n_{Fe}, and n_S are the numbers of Cu, Fe, and S atoms removed from the stoichiometric system to create the defects. For example, n_{Cu}, n_{Fe}, and n_S are −1, +1, and 0, respectively, for a surface with a single Cu-on-Fe antisite defect.

The existence of $CuFeS_2$ in chemical equilibrium constrains the sum $\mu_{Cu} + \mu_{Fe} + 2\mu_S$ to the heat of formation of $CuFeS_2$. We used the experimental value of −1.8 eV for the heat of formation obtained by Johnson and Steele [45]. Table II lists seven sets of μ_{Cu}, μ_{Fe}, and μ_S values that were chosen to represent a wide range of growth conditions within this constraint. For each of the seven conditions, the surface formation of all stable surfaces was computed and used, through the Wulff construction [46,47], to predict an equilibrium crystallite morphology. The Wulff constructions were generated and visualized using the software package DL-VISUALISE [48].

III. RESULTS

A. Nonpolar surfaces

The (110), (102), and (114) nonpolar surfaces have surface energies of 0.58, 0.61, and 0.66 J m^{-2}, respectively. The natures of the relaxations of these surfaces are found to have some general features in common; surface metal cations significantly displace inwards towards the bulk, while surface anion species relax slightly outwards towards the surface. As an illustration, the unrelaxed and relaxed configurations of the (110) surface are shown in Fig. 3. This relaxation pattern serves to increase the stability of surfaces in two ways. First, it alleviates undercoordination of surface cations through enhanced metal-metal (Cu-Fe, Cu-Cu, and Fe-Fe) interactions. Second, the tendency of the surface Cu and Fe cations to relax towards the bulk exposes S anions at the surface whose relatively large and polarizable electron clouds can provide electrostatic screening of the smaller metal cations. These general features of surface relaxation are typical for zinc-blende binary semiconductors such as ZnO and have been reported in DFT-LDA calculations of $CuInSe_2$ [19,20] and DFT-GGA calculations of $CuFeS_2$ [25]. For this class of materials, the (110) surface is found to be the most stable nonpolar surface [16–18,49]. This is consistent with the data presented here.

B. The defect-free polar (112)/($\overline{1}\overline{1}2$) surface pair

The defect-free configuration [configuration (a)] of the (112)/($\overline{1}\overline{1}2$) surface pair has a surface formation energy of 0.61 J m^{-2}, which means its thermodynamic stability is similar to that of the nonpolar (110), (102), and (114) surfaces. Even though the surface pair is polar (Tasker type 3), its thermodynamic stability is not surprising because the separation, perpendicular to the surface, of the cation and anion atomic layers within each repeating unit (~0.9 Å) is much shorter than the average bond length (~2.4 Å), which means the (112)/($\overline{1}\overline{1}2$) surface pair can be considered "weakly polar." While the stabilization mechanism of the nonpolar surfaces is mainly geometric, stabilization of the (112)/($\overline{1}\overline{1}2$) surface pair is attributed to a combination of geometric and electronic mechanisms.

The unrelaxed and relaxed configurations of the metal-terminated (112) surface are shown in Fig. 4. At the (112) surface, all four surface metal cations are displaced significantly (~0.80 Å) into the bulk, while two of the S anions in the subsurface layer relax outwards to the surface (~0.40 Å), resulting in a partial swap of the unrelaxed surface and subsurface layers. The purpose of the geometric relaxation at the (112) surface is similar to that of the nonpolar surfaces; the coordination of the undercoordinated surface metal cations is increased, and electrostatic screening of them is enhanced through exposure of S anions at the surface. Conversely, there is relatively little relaxation at the anion-terminated ($\overline{1}\overline{1}2$) surface, which is unsurprising since the subsurface metal cations are not undercoordinated and the geometry of the surface already facilitates electrostatic screening of the cations by S anions.

The electronic mechanism which stabilizes the (112)/($\overline{1}\overline{1}2$) surface pair involves charge transfer which is apparent in the density of states (DOS) plots and can be estimated using

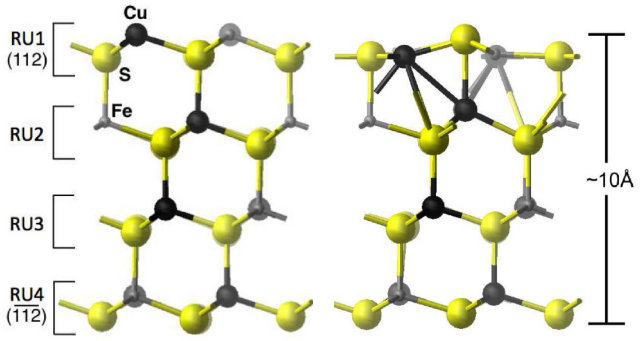

FIG. 4. (Color online) (a) The unrelaxed and (b) relaxed defect-free polar (112)/($\overline{1}12$) slab. The (112) surface is at the top, while the ($\overline{1}12$) surface is at the bottom. The four repeating units (RU) are also labeled.

Mulliken population analysis. The total and projected DOS of bulk $CuFeS_2$ and that of the (112)/($\overline{1}12$) surface pair are plotted in Fig. 5. The DOS of the surface pair are further projected onto atoms of the four repeating units [labeled in Fig. 4(a)] and shown in Fig. 6. The Fermi level is at 0.0 eV for all plots. For both plots the projection is onto all Fe atoms of the unit cell (for Fig. 5) or repeating unit (for Fig. 6). As $CuFeS_2$ is antiferromagnetic, the DOS is spin symmetric.

For bulk $CuFeS_2$, the bottom of the conduction band consists of mainly empty $3d$ Fe states, with a small contribution from $3p$ S states. The corresponding occupied $3d$ Fe states are in the range of -6.7 to -6.3 eV. The localized nature of these bands with little hybridization indicates that Fe-S bonds are strongly ionic. The occupied $3d$ Cu states are spread in the valence band between -4.0 eV and the Fermi level over several bands. A band of strongly ionic $3d$ Cu states can be identified in the range of -1.8 to -1.4 eV. Another band, slightly hybridized with $3p$ S states, is present between -1.4 eV and the Fermi level. Finally, a couple of bands of $3d$ Cu states strongly hybridized with $3p$ S states are found in the range -3.9 to -2.4 eV. The mixture of ionic and hybridized states suggests that Cu-S bonds are only partially ionic.

There are two key differences in the DOS of the polar (112)/($\overline{1}12$) surface pair compared to the bulk DOS. First, at the ($\overline{1}12$) surface (RU4), band gap states consisting of a mixture of $3d$ Cu and $3p$ S states can be identified between 1.0 and 1.2 eV. These states are also present in the central layers (RU2 and RU3) of the slab but at a lower intensity. Second, at the top of the valence band of the (112) surface a narrow band of $3d$ Fe states, originating from the bottom of the conduction band in the bulk, can be observed. These two features, considered in conjunction, are evidence that charge is transferred across the slab, mainly from the Cu and S atoms of the ($\overline{1}12$) surface to Fe atoms of the (112) surface.

Other differences in the DOS suggest that the nature of bonding in the surface pair is slightly different. Increased hybridization of $3d$ Cu and $3p$ S states can be observed throughout the whole slab, which suggests an increase in the degree of covalency of Cu-S bonds in the polar surface relative to the bulk. At the (112) surface (RU1), the occupied $3d$ Fe states shift further up in the energy up to the valence band, resulting in strong hybridization with $3p$ S states, which again suggests increased covalency. At the ($\overline{1}12$) surface (RU4), the occupied $3d$ Fe states are shifted up in energy by 0.5 eV compared with the bulk. This can be attributed to increased electrostatic repulsion due to contraction of surface Fe-S bonds and polarization of the S electron cloud towards the bulk upon surface cleavage. However, as the states are still strongly localized, it can be concluded that the Fe-S bonds in ($\overline{1}12$) remain strongly ionic.

Mulliken population analysis allows numerical estimation of the charge transferred. Relative to the bulk, Fe species at the (112) surface gained, on average, $0.17|e|$ per atom, while overall the surface as a whole (RU1) gained a total of $0.30|e|$ per unit cell. For the ($\overline{1}12$) surface, S and Cu species lost $0.20|e|$ per atom and $0.03|e|$ per atom, on average, respectively, while the surface as a whole (RU4) lost a total of $0.83|e|$ per unit cell. Using the Mulliken charges calculated for the bulk system, a pure electrostatic argument predicts that a surface-to-surface charge transfer of $1.29|e|$ per unit cell across the slab is required to suppress the macroscopic electrostatic

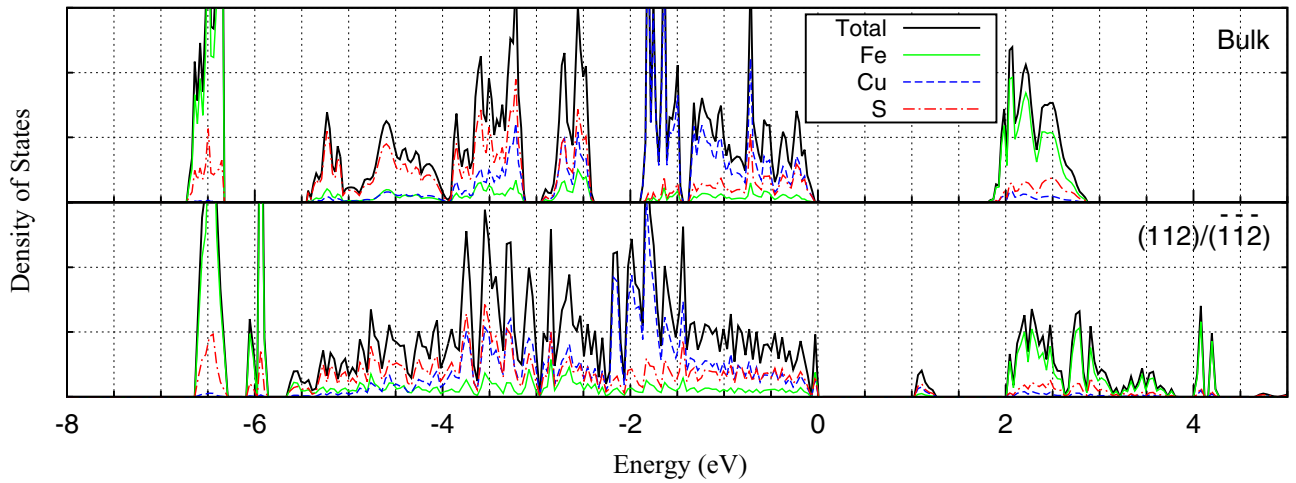

FIG. 5. (Color online) Total and projected density of states (DOS) for (top) bulk and (bottom) the (112)/($\overline{1}12$) surface pair of $CuFeS_2$. The DOS is projected onto Cu, Fe, and S species. The Fermi level is at 0.0 eV.

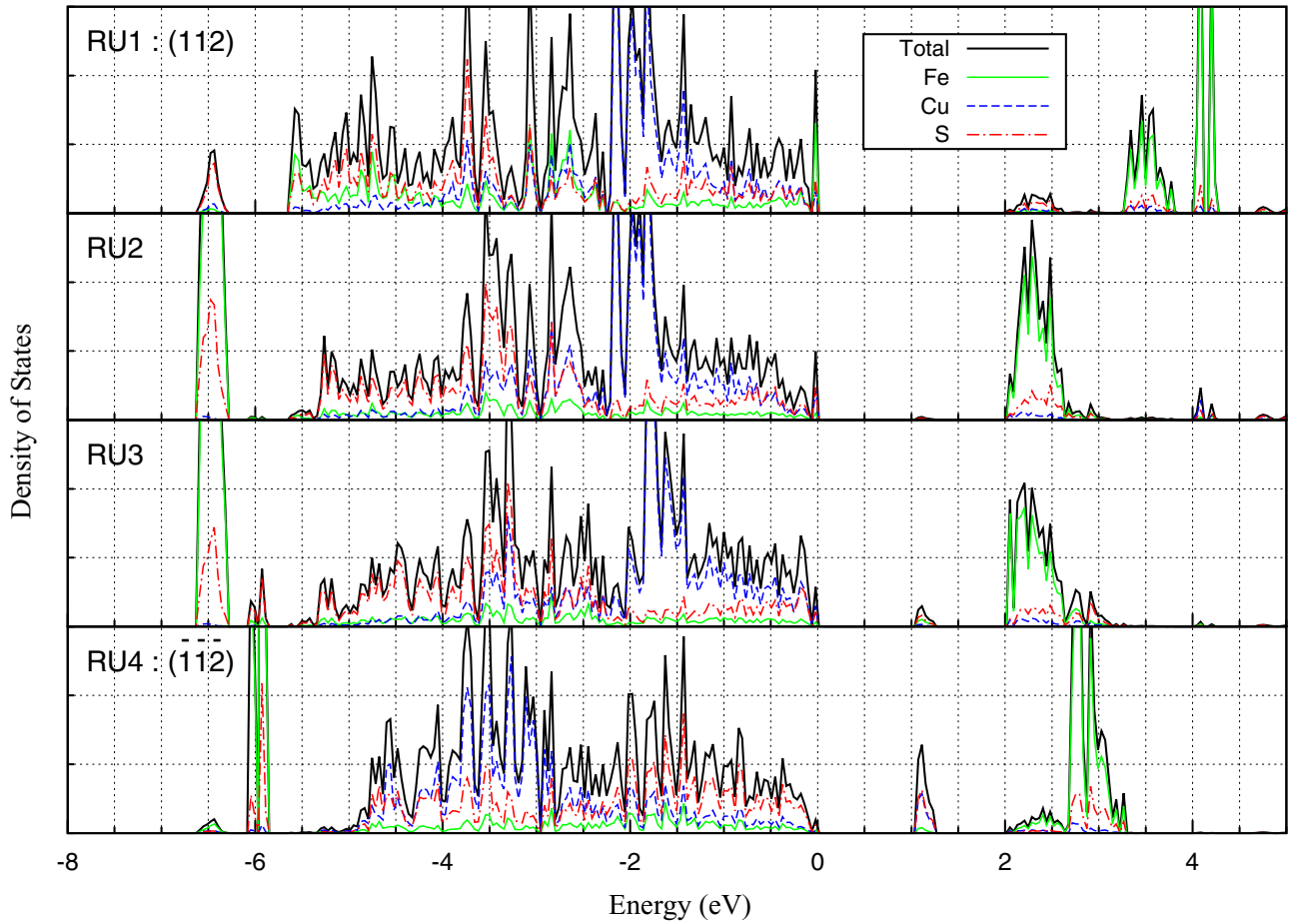

FIG. 6. (Color online) Total and projected DOS for each the four repeating units, defined in Fig. 4(a), of the (112)/(1$\bar{1}\bar{2}$) surface pair of $CuFeS_2$. The DOS is projected onto Cu, Fe, and S species. The Fermi level is at 0.0 eV.

dipole in the surface pair. As the estimated total charge transfer loss from atoms in the (1$\bar{1}\bar{2}$) surface is close to this value, it can be concluded that stabilization of the macroscopic field at the (1$\bar{1}\bar{2}$) surface is indeed mostly electronic. The difference between the required and estimated charge loss from atoms in the (1$\bar{1}\bar{2}$) surface to stabilize the macroscopic dipole can be accounted for by the imperfect ionicity of the system and possibly an additional stabilization mechanism involving change in the degree of covalency in surface bonds.

To summarize, the (112)/(1$\bar{1}\bar{2}$) surface pair is stabilized by a combination of geometric and electronic mechanisms. The geometric mechanism, localized to the (112) surface, involves significant geometry relaxation which exposes S anions that can then electrostatically screen the densely charged metal cations underneath. The electronic mechanism involves charge transfer predominantly from S species at the (1$\bar{1}\bar{2}$) surface to Fe species at the (112) surface. In addition, increased covalency in Cu-S and Fe-S bonds may also play a role. Collectively, these processes serve to stabilize the surface pair by suppressing the electric dipole moment perpendicular to the slab, as illustrated in the plot of the computed planar averaged potential across the slab in Fig. 7. The plot shows that the gap between the potential at the (112) and (1$\bar{1}\bar{2}$) surfaces, a measure of the electrostatic dipole across the surface, is almost eliminated during relaxation.

C. The polar (112)/(1$\bar{1}\bar{2}$) surface pair with defects

The data in Table III establish that under most growth conditions, further stabilization of the (112)/(1$\bar{1}\bar{2}$) surface pair can be achieved with the formation of defects. With the exception of Fe-poor conditions (condition E), the (112)/(1$\bar{1}\bar{2}$)

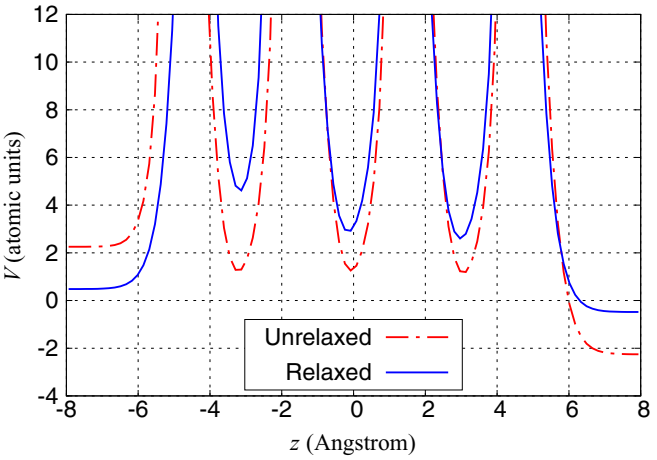

FIG. 7. (Color online) Planar averaged potential of the unrelaxed and relaxed defect-free (112)/(1$\bar{1}\bar{2}$) slab. The (112) surface is at positive z, while the (1$\bar{1}\bar{2}$) surface is at negative z.

TABLE III. Calculated surface energies of (112)/($\overline{1}\overline{1}2$) with the different defect configurations investigated at the seven growth conditions (A–G) defined in Table II. The surface energy of the (110) surface, the most stable nonpolar surface, is also shown for comparison. The surface energies are in J m^{-2}. For each growth condition, the lowest surface energy is in bold.

Configuration	Defect(s) on (112)	Defect(s) on ($\overline{1}\overline{1}2$)	A	B	C	D	E	F	G
(a)	None	None	0.61	0.61	0.61	0.61	0.61	0.61	0.61
(b)	2 × Cu vacancies	None	0.33	0.61	0.71	0.76	0.90	0.90	0.90
(c)	Cu, Fe vacancy pair	None	1.02	1.02	1.21	1.16	1.11	1.21	1.30
(d)	Cu-on-Fe antisite	None	1.12	0.84	0.93	0.84	0.65	0.74	0.84
(e)	None	Fe-on-Cu antisite	**0.22**	**0.50**	**0.41**	**0.50**	0.69	0.60	**0.50**
(f)	None	S adatom	0.65	0.65	0.75	0.72	0.65	0.75	0.80
(g)	None	S addimer	0.53	0.53	0.72	0.67	**0.53**	0.72	0.82
(h)	S adatom	S vacancy	0.71	0.71	0.71	0.71	0.71	0.71	0.71
(110) surface	N/A	N/A	0.58	0.58	0.58	0.58	0.58	**0.58**	0.58

surface pair with a Fe-on-Cu antisite on ($\overline{1}\overline{1}2$) [configuration (e)] is lower in energy than its defect-free equivalent. Furthermore, the defect-stabilized surface pair is thermodynamically preferred over the nonpolar (110) surface under those conditions apart from Cu-rich conditions (condition F). In particular, under Cu-poor conditions (condition A), its surface energy of 0.22 J m^{-2} is the lowest out of all surface energies computed. The presence of an S addimer at the ($\overline{1}\overline{1}2$) surface [configuration (g)] also has a stabilizing effect under Cu-poor, S-rich, and Fe-poor conditions (conditions A, B, and E). Under these conditions, the (112)/($\overline{1}\overline{1}2$) surface pair with a S addimer at the ($\overline{1}\overline{1}2$) surface is also thermodynamically preferred to the (110) surface. Out of all the defect configurations at the (112) surface investigated, only a pair of Cu vacancies [configuration (b)] stabilizes the (112)/($\overline{1}\overline{1}2$) surface pair and only under Cu-poor conditions (condition A). However, under these conditions, the surface energy is remarkably low at 0.33 J m^{-2}. All the other defects studied did not give rise to additional

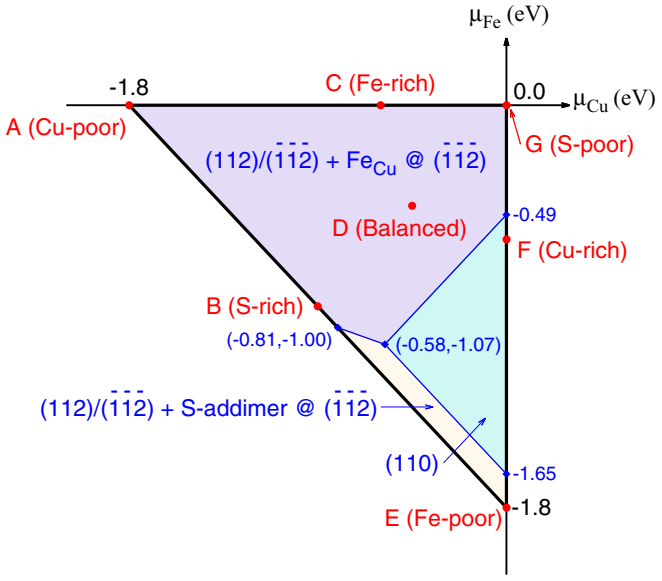

FIG. 8. (Color online) Phase diagram showing the most stable surface for all combinations of chemical potentials within the constraint $\mu_{Cu} + \mu_{Fe} + 2\mu_S = -1.8$ eV. The seven points (A–G) representing the growth conditions in Table II are marked.

thermodynamic stability of the (112)/($\overline{1}\overline{1}2$) surface pair under any realistic environmental conditions. Figure 8 is a "phase diagram" which shows the most stable surface as a function of the atomic chemical potentials. It shows that except for Cu-rich conditions, the defect-stabilized (112)/($\overline{1}\overline{1}2$) surface pair is more stable than the (110) surface.

D. Surface morphology of $CuFeS_2$

The proportion of different facets in the Wulff construction at growth conditions A–G in Table II is shown in Table IV. As the stability of the defect-stabilized (112)/($\overline{1}\overline{1}2$) surface pair varies widely with respect to the (nonstoichiometric) defect(s) and hence the growth conditions, the surface morphology also depends heavily on the growth conditions. Under Fe-rich or Cu-poor conditions (conditions A and C) an Fe-on-Cu antisite defect at the (112) surface stabilizes the (112)/($\overline{1}\overline{1}2$) surface pair to such an extent that the Wulff construction predicts a crystallite exclusively formed of (112) and ($\overline{1}\overline{1}2$) facets. Under Fe-poor conditions (condition E), the (112) and ($\overline{1}\overline{1}2$) facets still have the highest proportional area, with decreasing, but non-negligible, contributions from the nonpolar (110), (102), and (114) facets. Cu-rich conditions (condition F) give rise to the "richest" Wulff construction, with no family of facets having a proportional area of more than 40%. For the other three conditions (conditions B, D, and G), the (112) and ($\overline{1}\overline{1}2$) facets dominate, with a small combined contribution (~13%) from the nonpolar surfaces. As an illustration of the strong influence that the growth conditions have on the surface morphology, the Wulff constructions for copper-rich

TABLE IV. Proportional area (in %) of facets in the Wulff constructions created at the seven predetermined sets of atomic chemical potentials in Table II. Note that for the (112)/($\overline{1}\overline{1}2$) surface pair, the exact atomic configuration at the surface depends on the conditions (refer to Table III).

	A	B	C	D	E	F	G
(110)	0.0	10.3	0.0	10.3	17.9	31.2	10.3
(102)	0.0	1.6	0.0	1.6	8.5	18.5	1.6
(114)	0.0	1.0	0.0	1.0	3.1	10.4	1.0
(112)/($\overline{1}\overline{1}2$)	100.0	87.2	100.0	87.2	70.5	39.8	87.2

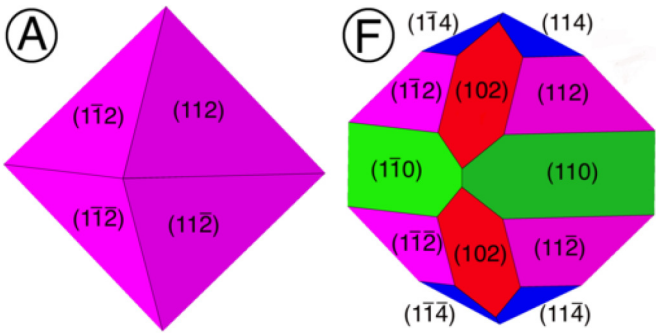

FIG. 9. (Color online) Wulff constructions of $CuFeS_2$ under growth conditions A (Cu poor) and F (Cu rich) defined in Table II. Due to the symmetry of the system, (hkl) is equivalent to $(\bar{h}kl)$, $(h\bar{k}l)$, and $(\bar{h}\bar{k}l)$.

and copper-poor conditions are shown in Fig. 9. From the data presented, it can be concluded that regardless of the growth conditions, defect-stabilized polar (112) and $(\bar{1}\bar{1}2)$ facets are likely to form a significant portion of $CuFeS_2$ crystallites.

IV. CONCLUSION

We have presented an *ab initio* study of the crystallite morphology, surface composition, and structure for a range of (1×1) $CuFeS_2$ surfaces as a function of the atomic chemical potentials. Our calculations show that the (110) surface is the most stable nonpolar surface, with a surface energy of 0.58 J m^{-2}, while the (102) and (114) surfaces are also low in energy (0.61 and 0.66 J m^{-2}, respectively). We also found the relaxed polar defect-free $(112)/(\bar{1}\bar{1}2)$ surface pair to be thermodynamically stable, with a surface formation energy similar to that of the nonpolar (110), (102), and (114) surfaces. The surface pair was stabilized during geometry relaxation due to a combination of electronic and geometric mechanisms that combine to suppress the electrostatic dipole perpendicular to the surface. Specifically, the $(\bar{1}\bar{1}2)$ surface was stabilized via transfer of charge to the (112) surface, while the (112) surface was additionally stabilized by a combination of geometric and electronic rearrangement. The $(112)/(\bar{1}\bar{1}2)$ surface pair can be further stabilized by the formation of defects to an extent that makes it thermodynamically preferred over the nonpolar (110) surface in the following scenarios: (a) two copper vacancies at the (112) surface, under Cu-poor conditions, (b) a S addimer at the $(\bar{1}\bar{1}2)$ surface, under Cu-poor, Fe-poor, or S-rich conditions, and (c) a Fe-on-Cu antisite at the $(\bar{1}\bar{1}2)$ surface, under all conditions except for Fe-poor or Cu-rich conditions. Through Wulff constructions generated for a wide range of reasonable growth conditions, we conclude that within the bounds of this work, defect-stabilized (112) and $(\bar{1}\bar{1}2)$ facets will always form a significant constituent of the surface morphology regardless of the growth conditions.

ACKNOWLEDGMENTS

V.H.-Y.C. was supported through a studentship in the Centre for Doctoral Training on Theory and Simulation of Materials at Imperial College London, funded by the Engineering and Physical Sciences Research Council (EPSRC) of the United Kingdom under Grant No. EP/G036888/1. R.M.-C. would like to thank the Ministerio de Economía y Competitividad (Spain) for a Juan de la Cierva Fellowship. This work was supported by the Rio Tinto Centre for Advanced Mineral Recovery at Imperial College London. This work made use of the high-performance computing facilities of Imperial College London and, via our membership to the United Kingdom's HPC Materials Chemistry Consortium, which is funded by the EPSRC (Grant No. EP/L000202), of the ARCHER UK National Supercomputing Service.

[1] E. M. Cordoba, J. A. Munoz, M. L. Blazquez, F. Gonzalez, and A. Ballester, Hydrometallurgy **93**, 81 (2008).
[2] S. Wang, JOM **57**, 48 (2005).
[3] R. Garlapalli, E. H. Cho, and R. Yang, in *Hydrometallurgy 2008: Proceedings of the 6th International Symposium* (Society for Mining Metallurgy & Exploration, Colorado, USA, 2008), p. 653.
[4] J. C. Fuentes-Aceituno, G. T. Lapidus-Lavine, and J. González, in *Hydrometallurgy 2008: Proceedings of the 6th International Symposium* (Society for Mining Metallurgy & Exploration, Colorado, USA, 2008), p. 664.
[5] N. Pradhan, K. C. Nathsarma, K. S. Rao, L. B. Sukla, and B. K. Mishra, Miner. Eng. **21**, 355 (2008).
[6] A. A. Baba, K. I. Ayinla, F. A. Adekola, M. K. Ghosh, O. S. Ayanda, R. B. Bale, A. R. Sheik, and S. R. Pradhan, Int. J. Min. Eng. Miner. Process. **1**, 1 (2012).
[7] P. B. Munoz, J. D. Miller, and M. E. Wadsworth, Metall. Trans. B **10**, 149 (1979).
[8] R. P. Hackl, D. B. Dreisinger, E. Peters, and J. A. King, Hydrometallurgy **39**, 25 (1995).
[9] M. Ammou-Chokroum, M. Cambazoglu, and D. Steinmez, Bull. Soc. Fr. Miner. Cristallogr. **100**, 161 (1977).
[10] Å. Sandström, A. Shchukarev, and J. Paul, Miner. Eng. **18**, 505 (2005).
[11] G. U. V. Oertzen, S. L. Harmer, and W. M. Skinner, Mol. Simul. **32**, 1207 (2006).
[12] Y. Li, A. P. Chandra, and A. R. Gerson, Geochim. Cosmochim. Acta **133**, 372 (2014).
[13] R. Martinez-Casado, V. H.-Y. Chen, G. Mallia, and N. M. Harrison (unpublished).
[14] S. R. Hall and J. M. Stewart, Acta Crystallogr. Sect. B **29**, 579 (1973).
[15] P. W. Tasker, J. Phys. C **12**, 4977 (1979).
[16] W. Monch, *Semiconductor Surfaces and Interfaces*, Springer Series in Surface Science Vol. 16 (Springer, Berlin, 1995).
[17] M. Lannoo and P. Friedel, *Atomic and Electronic Structure of Surfaces*, Springer Series in Surface Science Vol. 26 (Springer, Berlin, 1991).
[18] F. Bechstatd and R. Enderlein, *Semiconductor Surfaces and Interfaces* (Akademie-Verlag, Berlin, 1988).
[19] J. E. Jaffe and A. Zunger, Phys. Rev. B **64**, 241304 (2001).
[20] S. B. Zhang and S.-H. Wei, Phys. Rev. B **65**, 081402 (2002).
[21] D. Liao and A. Rockett, J. Appl. Phys. **91**, 1978 (2002).

[22] C. de Oliveira and H. A. Duarte, Appl. Surf. Sci. **257**, 1319 (2010).
[23] C. Klauber, Surf. Interface Anal. **35**, 415 (2003).
[24] C. Klauber, Surf. Interface Anal. **35**, 770 (2003).
[25] C. de Oliveira, G. F. de Lima, H. A. de Abreu, and H. A. Duarte, J. Phys. Chem. C **116**, 6357 (2012).
[26] G. F. de Lima, C. de Oliveira, H. A. de Abreu, and H. A. Duarte, J. Phys. Chem. C **115**, 10709 (2011).
[27] G. F. de Lima, C. de Oliveira, H. A. de Abreu, and H. A. Duarte, Int. J. Quantum Chem. **112**, 3216 (2012).
[28] R. Dovesi, R. Orlando, B. Civalleri, C. Roetti, V. R. Saunders, and C. M. Zicovich-Wilson, Z. Kristallogr. **220**, 571 (2005).
[29] R. Dovesi, V. R. Saunders, C. Roetti, R. Orlando, C. M. Zicovich-Wilson, F. Pascale, B. Civalleri, K. Doll, N. M. Harrison, I. J. Bush, P. D'Arco, and M. Llunell, *CRYSTAL09 User's Manual* (University of Torino, Torino, Italy, 2009).
[30] A. D. Becke, J. Chem. Phys. **98**, 5648 (1993).
[31] C. Lee, W. Yang, and R. G. Parr, Phys. Rev. B **37**, 785 (1988).
[32] D. Munoz, N. M. Harrison, and F. Illas, Phys. Rev. B **69**, 085115 (2004).
[33] G. Mallia and N. M. Harrison, Phys. Rev. B **75**, 165201 (2007).
[34] N. C. Wilson, S. P. Russo, J. Muscat, and N. M. Harrison, Phys. Rev. B **72**, 024110 (2005).
[35] L. Ge, J. H. Jefferson, B. Montanari, N. M. Harrison, D. G. Pettifor, and G. Briggs, ACS Nano **3**, 1069 (2009).
[36] G. C. De Fusco, L. Pisani, B. Montanari, and N. M. Harrison, Phys. Rev. B **79**, 085201 (2009).
[37] L. Liborio, G. Mallia, and N. M. Harrison, Phys. Rev. B **79**, 245133 (2009).
[38] C. L. Bailey, L. Liborio, G. Mallia, S. Tomić, and N. M. Harrison, Phys. Rev. B **81**, 205214 (2010).
[39] L. Liborio, C. L. Bailey, G. Mallia, S. Tomić, and N. M. Harrison, J. Appl. Phys. **109**, 023519 (2011).
[40] S. Tomi, C. Montanari, and N. M. Harrison, Phys. E (Amsterdam, Neth.) **40**, 2125 (2008).
[41] H. Xiao, J. Tahir-Kheli, and W. A. Goddard, J. Phys. Chem. Lett. **2**, 212 (2011).
[42] A. Alkauskas, P. Deák, J. Neugebauer, A. Pasquarello, and C. G. Van de Walle, *Advanced Calculations for Defects in Materials: Electronic Structure Methods* (Wiley-VCH, Weinheim, 2011).
[43] C. Pisani, R. Dovesi, and C. Roetti, *Hartree-Fock ab initio Treatment of Crystalline Systems* (Springer, Heidelberg, 1988).
[44] M. W. Finnis, Phys. Status Solidi A **166**, 397 (1999).
[45] G. K. Johnson and W. V. Steele, J. Chem. Thermodyn. **13**, 991 (1981).
[46] G. Wulff, Z. Kristallogr. **34**, 449 (1901).
[47] M. von Laue, Z. Kristallogr. **105**, 124 (1943).
[48] B. G. Searle, Comput. Phys. Commun. **137**, 25 (2001).
[49] N. Moll, A. Kley, E. Pehlke, and M. Scheffler, Phys. Rev. B **54**, 8844 (1996).